GSA DATA REPOSITORY 2014341

Supplement to:

Geomorphology of Lunar Grabens Requires Igneous Dikes at Depth

Christian Klimczak

TOPOGRAPHIC PROFILES AND NUMERICAL SIMULATIONS

Topographic data used and rationale for analyzed grabens

Topographic profiles in Schrödinger basin (profiles 1 to 4) were extracted from the gridded 1024 ppd LOLA product (http://imbrium.mit.edu/BROWSE/LOLA_GDR/CYLINDRICAL.html), and topographic measurements from individual LOLA tracks were extracted from the Lunar Orbital Data Explorer (http://ode.rsl.wustl.edu/moon/indextools.aspx) for Rimæ Daniell (profiles D5 and D6) and other ~E-W oriented graben structures (see below). Original profiles show a 0.5° to 1° slope (Figure 2, thin blue line), that is shown with 35 times exaggeration in all profiles. Linear slopes were obtained from the relationship between the topographic difference and the horizontal distance of the first to the last data point in the extracted profile. All profiles were then detrended by removing the linear slope (Figure 2, thick blue line) to allow for better comparison to ground displacement simulations.

In the polar regions (e.g., examples for Schrödinger basin), LOLA coverage is dense so that the gridded LOLA product is of sufficient resolution for topographic profiles across grabens to be extracted and analyzed without too many interpolation artifacts. The gridded product is of insufficient resolution in the mid-latitudes and equatorial regions, as too many interpolation artifacts affect topographic profiles, especially if they are taken in the N−S direction. Individual LOLA tracks, which are oriented N−S due to the polar orbit of the Lunar Reconnaissance Orbiter (LRO) spacecraft, are required for an analysis instead. This then limits an analysis to more or less E−W oriented grabens in these regions.

The analysis of lunar grabens in this study was also limited to only the most prominent structures (widest and deepest troughs) that meet criteria for data coverage and data resolution (see above). All suitable examples were topographically evaluated. They occur in various geologic settings (edge of mascon basins, periphery of maria, on the floors of impact basins) and across the entire lunar surface (northern mid-latitudes, equator, southern mid-latitudes, and south polar region) so that this study can be considered planet-wide. Planet-wide, all grabens suited for the analysis have the potential to be underlain by a dike.

Sample standard deviations between the topographic profiles and simulations

Ground displacements were simulated using the open-source code COULOMB (Lin and Stein, 2004; Toda et al., 2005) run in MatLab®, by specifying and varying geometric properties of a graben alone (Figure DR1A), dike alone, and dike−graben combination (Figure DR1B) until a visually good fit is obtained. Good fits to topographic

profiles are only achieved for a narrow range of geometric properties, giving confidence that simulated structures are good approximations of structures present on the Moon.

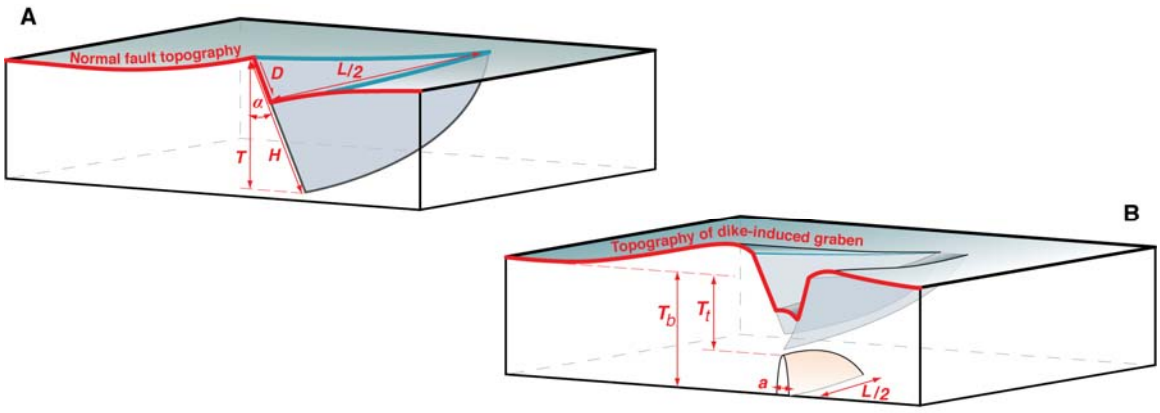

Figure DR1. Stylized geomorphology of planetary graben settings. A) Planetary half-graben geomorphology is comprised of a gentle synclinal flexure in the rock units below the fault plane (i.e., foot wall syncline) as well as a gentle anticlinal flexure in the rock units above the fault plane (i.e., hanging wall anticline). Topographic extent and range of the landform, as well as degree of flexure of rock units are governed by the fault geometry, including fault length (L), fault height (H), fault displacement (D), fault dip (α) and depth of faulting (T). B) Dike-related graben geomorphology is governed by normal fault geometric properties as well as geometry of the underlying dike. The dike geometry is characterized by dike width or aperture (a), dike length (L), and depth below surface to the top (T_t) and approximate bottom (T_b) of the dike. The difference between T_t and T_b equates to the height, H, of the dike.

To assess the goodness of fit between the topography and the simulated ground displacements, a standard sample deviation (s) was calculated. The sample standard deviation is given as:

$$s = \sqrt{\frac{1}{N-1}\sum_{i=1}^{N}\left(x_i - \bar{x}\right)^2}, \qquad (1)$$

where N is the total number of simulated data points. The term $\left(x_i - \bar{x}\right)$ represents the residuals between simulation and observation, with x_i being the i^{th} data point of the simulation, and $\bar{x}$ being the topographic value at the i^{th} datapoint that is tried to be matched with x_i. Values of s provide a measure of the average deviation of simulated ground displacements from the topography, and thus simulations with a lower s have a better fit. Residuals for profile S(4) (Figure 2) are given as example (Figure DR2). Residuals for the graben fit are small at or near the graben but become larger further away from the structure. In general, dike and dike-related graben fits have much lower residuals throughout the entire profile. However, the ruggedness of the topography affects sample standard deviations, showing that more rugged topographies cannot be as accurately recreated by numerical models as topographically smoother areas (Figure 2),

and thus it is difficult to compare the goodness of fit for simulated ground displacements between different profiles with the sample standard deviations alone.

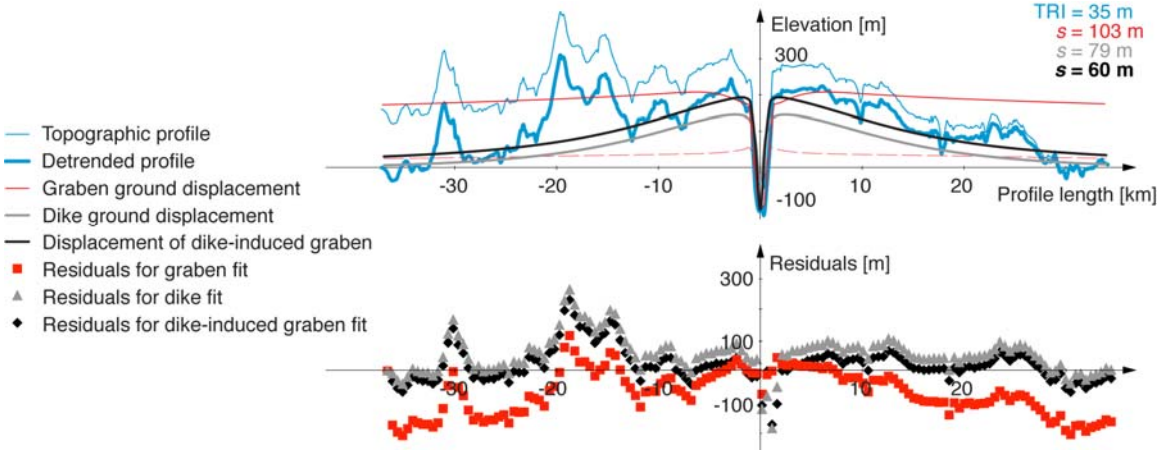

Figure DR2. Ground displacement simulations and topography for profile S(4) (top) and corresponding residuals between the models and observed topography (bottom). Note that the residuals are highest in the topographically most rugged portion of the profile.

Two-dimensional Topographic Ruggedness Index (TRI)

The topographic ruggedness index (TRI) is a measure of the average amount of elevation difference between adjacent topographic measurements in a digital elevation model (Riley et al., 1999). For three-dimensional datasets, the TRI is the average of the absolute values of the elevation difference from a center cell and the eight cells immediately surrounding it. For two-dimensional elevation data (i.e., topographic profiles), this algorithm was modified to solve for the average of the absolute values of the elevation difference of the neighboring data points, expressed as:

$$TRI = \sqrt{\frac{1}{N}\sum_{i=1}^{N}\left(x_i - x_{i+1}\right)^2}\,. \qquad (2)$$

Here, N is the total number of topographic measurements, x_i is the i^{th} topographic measurement of the profile, and x_{i+1} is the topographic measurement neighboring x_i. As the TRI value defines the average change of elevation between measurements within the topographic profile, the s values should not exceed the TRI values for a simulated fit to be considered as "good", as sample standard deviations of the models are then smaller than the average natural variation in the observational data. This rule allows for larger sample standard deviations in more rugged terrains and demands smaller sample standard deviations in smoother terrains, thus enabling comparison of goodness of fits between different types of terrain.

Elevation differences between neighboring measurements are again given for profile S(4) as example (Figure DR3). Generally, the changes in elevation between neighboring measurements over the entire profile are rather low, mostly below 10 m and

in the more rugged regions between 20 and 40 m. The graben at the origin of the diagram is the most rugged landform of the entire topographic profile with 150 m change between measurements. The left portion of the profile is more rugged than the right portion, caused by rough hummocky basin floor material (Kramer et al., 2013). Therefore, the residuals between the models and observed topography are larger in the left portion than the right one (Figure DR2). The TRI value of this profile is 35 m. This value almost twice as low as the *s* value for the best-fit simulation of a dike-related graben. Generally, however, the residuals for this fit are quite low, especially on the right portion of the profile, where there is no rough geologic surface unit.

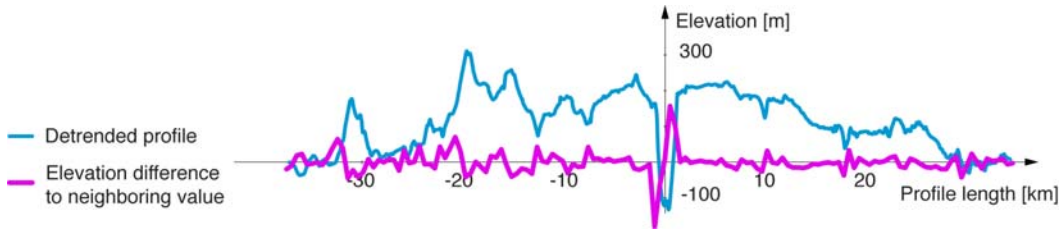

Figure DR3. Topographic profile S(4) and elevation difference of the neighboring data points.

ELASTIC PROPERTIES OF A FRACTURED LUNAR LITHOSPHERE

The lunar lithosphere very likely consists of a combination of intact rock and associated structural weaknesses, such as fractures, impact damage zones, and lithologic contacts that together weaken the overall material. The rock mass rating (RMR) system, measured on a scale from 0 to 100, where 100 represents intact rock, is frequently used in geo-engineering and geomechanics applications to account for the degree and condition of weaknesses (as well as for pore pressure conditions) within a rock (Bieniawski, 1989) to better evaluate elastic rock properties on lithospheric scales (Schultz, 1993, 1995, 1996).

Elastic rock properties include Young's Modulus, E, and the related Shear Modulus (μ). Either one of these properties is required to calculate magma overpressures (P) within a dike (Figure 3) using the relation (Rubin, 1995):

$$a = \frac{(P - \sigma_h)}{\mu/(1-\nu)} 1/2\, H, \tag{3}$$

with ν being Poisson's Ratio and σ_h being the surrounding stress. In a neutral tectonic regime, this stress is equal to the confining pressure (overburden). Young's Modulus and the Shear Modulus depend on confining pressure that increases with depth, z. For conditions appropriate for Earth this is estimated as (Schultz et al., 2006):

$$E = E^* + z^{0.4}, \tag{4}$$

where E^* denotes the Deformation Modulus. Empirical studies found that E^* is relatively insensitive to rock type, and that it relates to RMR as:

$$E^* = 2\,\mathrm{RMR} - 100 \qquad \text{for RMR} > 50 \qquad (5a)$$

and

$$E^* = 10^{(\mathrm{RMR}-10)/40} \qquad \text{for RMR} < 50, \qquad (5b)$$

with the units of E^* given in GPa (Bieniawski, 1989). Deformation Moduli for rock masses of moderate quality (RMR 55) are ~10 GPa, Deformation Moduli of rock masses of poor quality (RMR 35 to 45), such as expected for the heavily fractured upper lunar lithosphere (Wieczorek et al., 2013), are 4.2 to 7.5 GPa.

The depth dependent Deformation Modulus (Eq. 4) on other rocky bodies is then obtained by using a scaling relation (Schultz et al., 2006) given as:

$$E = E^* + \left(\frac{g}{g_{Earth}}\right)\left(\frac{\rho}{\rho_{Earth}}\right) z^{0.4}, \qquad (6)$$

where the term $\left(\frac{g}{g_{Earth}}\right)$ is the normalized surface gravitational acceleration and the term $\left(\frac{\rho}{\rho_{Earth}}\right)$ is the normalized rock density (see details in Schultz et al., 2006). The depth dependent Deformation Modulus for conditions appropriate on the Moon (g = 1.6 m/s^2 and bulk density of the upper lithoshpere of $\rho \approx 2600$ kg/m^3 (Wieczorek et al., 2013)) can now be used to calculate magma overpressures (Eq. 3), if dike geometric properties (a, H) and surrounding stresses are known.

DIKE GEOMETRIES

Magma overpressures (Eq.3) were estimated for 10 dikes. Dike dimensions were inferred from ground displacement modeling of four structures inside Schrödinger basin (Figure 2), as well as from three structures along two profiles across Rimæ Daniell (Figure 2) and for Rima Ariadaeus, Rima Hyginus, and Rima Hesiodus (Figure DR4). Ground displacement fits for the latter three structures are presented in Figure DR5. Rima Ariadaeus is a topographically very pronounced and asymmetric graben. Rima Hyginus is also a topographically prominent graben structure. Both grabens show a structural relief of up to 450 m and lie on a topographic rise (Figure DR5), similar to grabens in Schrödinger basin. In addition, Rima Hyginus displays a series of volcanic pits and volcanic deposits following the structural trend of the graben (Wilson et al., 2011; Figure DR4). Both topographic profiles are best approximated with the ground displacements of a dike-related graben.

Rima Hesiodus is a ~280-km-long graben structure cutting through highlands and mare units (Figure DR4). Its structural relief of only 100 to 120 m is smaller than that of other lunar grabens of similar length. Modeled ground displacements of a graben alone

and a dike-related graben are equally good (Figure DR5), thus indicating that a dike could be present at depth but may not be invoked for this particular structure.

All potential dike-related grabens of this study, including the derived best-fit dike geometric properties are listed in Table DR1.

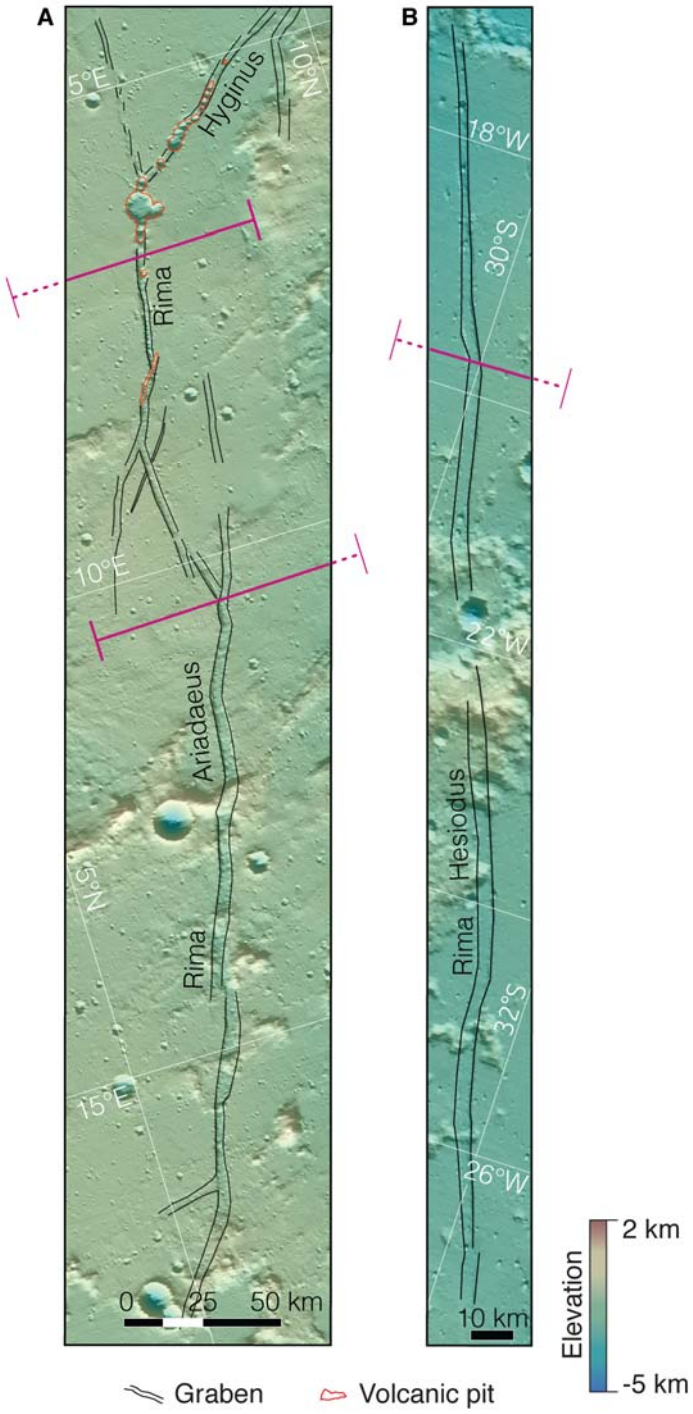

Figure DR4. Structural map overlaid on topography of Rima Ariadaeus and Rima Hyginus (A) as well as Rima Hesiodus (B). Extracted portions of LOLA tracks are indicated in pink.

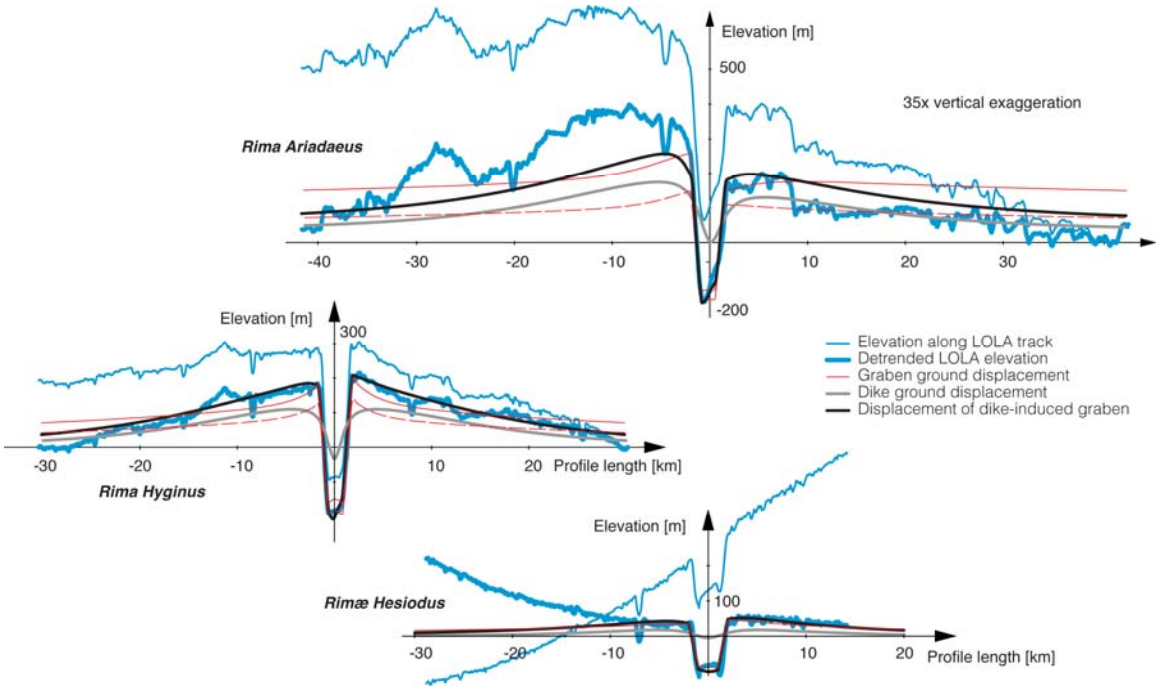

Figure DR5. Observed and detrended LOLA profiles (blue) across Rima Ariadaeus (from S to N), Rima Hyginus (S to N), and Rima Hesiodus (N to S) with simulated ground displacements of normal faults only (red) dikes (grey) and dike-related grabens (black). Rima Ariadaeus and Rima Hyginus are best matched with the ground displacement of a dike-related graben. Ground displacements of both graben alone and dike-related graben match the topography across Rima Hesiodus equally well.

Table DR1. Table of dike geometric properties derived from ground displacement simulations matched to LOLA topographic profiles.

Structure	Dike aperture, a	Depth to top of dike, T_t	Approximate depth to bottom of dike, T_b	Dike height, H
Schrödinger S(1)	400	0.5	5.5	5
Schrödinger S(2)	250	0.5	5.5	5
Schrödinger S(3)	400	0.3	15.3	15
Schrödinger S(3)	400	0.3	15.3	15
Schrödinger S(4)	500	0.3	14.3	14
Rima Daniell D(5)	500	0.1	10.1	10
Rima Daniell D(6)	200	0.35	8.85	8.5
Rima Daniell D(6)	300	0.3	10.3	10
Rima Ariadaeus A	550	2.5	20.5	18
Rima Hyginus Hy	500	1	19	18
Rima Hesiodus He	100	2	12	10

REFERENCES CITED

Bieniawski, Z.T., 1989, Engineering rock mass classifications: New York, Wiley.

Kramer, G.Y., Kring, D.A., Nahm, A.L., Pieters, C.M., 2013, Spectral and photogeologic mapping of Schrödinger Basin and implications for post-South Pole-Aitken impact deep subsurface stratigraphy: Icarus, v. 223, p. 131–148, doi: 10.1016/j.icarus.2012.11.008.

Lin, J., and Stein, R.S., 2004, Stress triggering in thrust and subduction earthquakes, and stress interaction between the southern San Andreas and nearby thrust and strike-slip faults: Journal of Geophysical Research, v. 109, B02303, doi:10.1029/2003JB002607.

Riley, S. J., DeGloria, S.D., and Elliot, R., 1999, A terrain ruggedness index that quantifies topographic heterogeneity: Intermountain Journal of Sciences, v. 5, no. 1–4, p. 23–27.

Schultz, R.A., 1993, Brittle strength of basaltic rock masses with applications to Venus: Journal of Geophysical Research, v. 98, p. 10883–10–895.

Schultz, R.A., 1995, Limits on strength and deformation properties of jointed basaltic rock masses: Rock Mechanics and Rock Engineering, v. 28, p. 1–15.

Schultz, R.A., 1996, Relative scale and the strength and deformability of rock masses: Journal of Structural Geology, v. 18, p. 1139–1149.

Schultz, R.A., Okubo, C.H., Wilkins, S., 2006, Displacement-length scaling relations for faults on the terrestrial planets: Journal of Structural Geology, v. 28, p. 2182–2193.

Toda, S., Stein, R.S., Richards-Dinger, K., and Bozkurt, S., 2005, Forecasting the evolution of seismicity in southern California: Animations built on earthquake stress transfer: Journal of Geophysical Research, v. 110, B05S16, doi:10.1029/2004JB003415.

Wieczorek, M.A., and 15 other, 2013, The Crust of the Moon as Seen by GRAIL: Science, v. 339, no. 6120, p. 671–674, doi:10.1126/science.1231530.

Wilson, L., Hawke, B.R., Giguere, T.A., Petrycki, E.R., 2011, An igneous origin for Rima Hyginus and Hyginus crater on the Moon: Icarus, v. 215, no. 2, p. 584–595.